In situ observation of active oxygen species in Fe-containing Ni-based oxygen evolution catalysts: the effect of pH on electrochemical activity

Trzesniewski, BJ; Diaz-Morales, O; Vermaas, DA; Longo, A; Bras, W; Koper, MTM; Smith, WA

DOI
10.1021/jacs.5b06814

Publication date
2015

Document Version
Final published version

Published in
Journal of the American Chemical Society

JACS
JOURNAL OF THE AMERICAN CHEMICAL SOCIETY
Article
pubs.acs.org/JACS

In Situ Observation of Active Oxygen Species in Fe-Containing Ni-Based Oxygen Evolution Catalysts: The Effect of pH on Electrochemical Activity

Bartek J. Trześniewski,[†,∥] Oscar Diaz-Morales,[‡,∥] David A. Vermaas,[†] Alessandro Longo,[§] Wim Bras,[§] Marc T.M. Koper,[‡] and Wilson A. Smith*[,†]

[†]Materials for Energy Conversion and Storage (MECS), Department of Chemical Engineering, Faculty of Applied Sciences, Delft University of Technology, 2628 BL Delft, The Netherlands

[‡]Leiden Institute of Chemistry, Leiden University, P.O. Box 9502, 2300 RA Leiden, The Netherlands

[§]Netherlands Organization for Scientific Research (NWO), The European Synchrotron Radiation Facility (ESRF), CS40220, 38043 Grenoble Cedex 9, France

Supporting Information

ABSTRACT: Ni-based oxygen evolution catalysts (OECs) are cost-effective and very active materials that can be potentially used for efficient solar-to-fuel conversion process toward sustainable energy generation. We present a systematic spectroelectrochemical characterization of two Fe-containing Ni-based OECs, namely nickel borate (Ni(Fe)−B_i) and nickel oxyhydroxide (Ni(Fe)OOH). Our Raman and X-ray absorption spectroscopy results show that both OECs are chemically similar, and that the borate anions do not play an apparent role in the catalytic process at pH 13. Furthermore, we show spectroscopic evidence for the generation of negatively charged sites in both OECs ($NiOO^-$), which can be described as adsorbed "active oxygen". Our data conclusively links the OER activity of the Ni-based OECs with the generation of those sites on the surface of the OECs. The OER activity of both OECs is strongly pH dependent, which can be attributed to a deprotonation process of the Ni-based OECs, leading to the formation of the negatively charged surface sites that act as OER precursors. This work emphasizes the relevance of the electrolyte effect to obtain catalytically active phases in Ni-based OECs, in addition to the key role of the Fe impurities. This effect should be carefully considered in the development of Ni-based compounds meant to catalyze the OER at moderate pHs. Complementarily, UV−vis spectroscopy measurements show strong darkening of those catalysts in the catalytically active state. This coloration effect is directly related to the oxidation of nickel and can be an important factor limiting the efficiency of solar-driven devices utilizing Ni-based OECs.

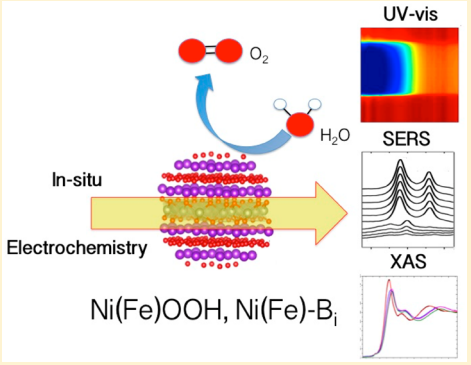

INTRODUCTION

The development of clean, efficient, and sustainable alternatives to fossil fuels has become one of the most pressing issues facing humanity today. Renewable electricity generation through solar and wind power could provide enough energy to power the planet for the foreseeable long-term future.[1−3] However, large-scale storage of the energy produced by such intermittent sources remains a major challenge. One of the most promising methods to store renewable electricity is through the electrolysis of water ($H_2O \rightarrow H_2 + 1/2\ O_2$). The hydrogen and oxygen produced via water electrolysis can be subsequently recombined in a fuel cell to produce electricity and water, thus making the overall energy conversion cycle complete.[3,4] In order to make this technology scalable, cheap, and efficient, catalysts are needed to drive the hydrogen and oxygen evolution reactions. The hydrogen evolution reaction implies the transfer of two protons and two electrons, and there are catalysts that can drive this reaction near to the equilibrium potential (0 V vs RHE).[5] However, the oxygen evolution reaction (OER) involves the transfer of four protons and four electrons, and it proceeds far from the equilibrium potential (1.23 V vs RHE), which causes large energy losses in the overall water splitting process.[5,6] Therefore, a focus on understanding the OER in order to improve its kinetics is paramount for enabling large-scale renewable energy storage.

Ni-based catalysts are one of the best alternatives[6−12] to the most active, yet prohibitively expensive catalysts based on scarcely abundant ruthenium and iridium oxides. Therefore, the anodes for large scale commercial alkaline electrolyzers are mostly based on nickel and its alloys.[13−15] Nickel-based OECs are known to oxidize water in alkaline media with activity comparable to RuO_2 and IrO_2 benchmark catalysts.[6−12] In particular, $Ni(OH)_2$/NiOOH has a beneficial three dimensionally porous brucite structure that facilitates easy ion transport and charge conductivity.[16] This catalyst has recently been used

Received: July 9, 2015
Published: November 6, 2015

DOI: 10.1021/jacs.5b06814
J. Am. Chem. Soc. 2015, 137, 15112−15121

in direct photoelectrochemical water splitting cells, where it forms a so-called adaptive junction when placed on semiconductor photoelectrodes.[17,18] In the past few years, a new form of this catalyst has been developed to form a nickel−borate (Ni−B_i) OEC.[19] This heterogeneous catalyst can be electrodeposited as a thin film from solutions containing $Ni_{(aq)}^{2+}$ and the proton-accepting borate anions. Ni−B_i can mediate the OER under mild conditions and with high activity.[20] It is believed that Ni−B_i is composed of nanosized, molecular-like clusters/domains of NiOOH, which results in a much larger fraction of surface-exposed, catalytically active nickel centers, relative to NiOOH.[21] However, a recent study from the Boettcher group finds that the activity of Ni−B_i is mainly due to the Fe impurities and not the Ni sites,[22] a result that is also consistent with previous findings of the beneficial role that Fe plays in the catalytic activity of pure NiOOH.[23−26] It is therefore important to note that previous Ni-based OEC systems demonstrating low onset potentials are actually reporting on materials that have some iron incorporated, as shown indisputably by the Boettcher group.[22,23] Therefore, given the importance of Fe for the OER activity, we assume that all the Ni-based OECs obtained in our study from nonpurified media should be referred to as Ni(Fe)OOH/Ni(Fe)−B_i.

To further understand the mechanisms and functionalities of these promising catalysts and to exploit the potential of their high catalytic activity, it is imperative to track the changes occurring in them during the OER reaction. Spectroelectrochemical characterization techniques allow to study in situ the processes at the electrode interface during the catalytic reaction without affecting the performance of the catalyst, and can therefore be used to track the changes in the nickel-based OECs during electrochemical water oxidation.

This work presents an electrochemical and UV−vis/Raman/XAS spectro-electrochemical study of the structural and electronic changes of Ni(Fe)OOH and Ni(Fe)−B_i catalysts during the electrochemical water oxidation reaction. Our results indicate that both Ni(Fe)OOH and Ni(Fe)-B_i structurally and electronically change in a very similar manner, indicating a similar composition, morphology, and physical characteristics. We also demonstrate a significant effect of electrolyte pH on the activity of both catalysts toward oxygen evolution. Surface Enhanced Raman Spectroscopy (SERS) measurements indicate the formation of negatively charged surface sites in the OECs (adsorbed "active oxygen") due to a deprotonation process. Those "active oxygen" species act as an OER precursor that explains the pH sensitivity of the OER catalytic activity. The deprotonation process has a crucial effect on the OER activity of Ni-based OECs at moderate pHs, which should be considered separate from the effect of the Fe impurities in the electrolyte, reported to enhance the catalytic activity of Ni-based electrocatalyst toward OER.[23,25,26]

EXPERIMENTAL SECTION

Preparation of Ni(Fe)−B_i and Ni(Fe)OOH Thin Films on FTO. Thin layers (~20 monolayers) of Ni(Fe)−B_i and Ni(Fe)OOH were electrodeposited on fluorine-doped tin oxide coated glass substrates (FTO, 15 Ω/cm, TEC-15, Hartford Glass Co.). Prior to the deposition process, substrates were cleaned by three successive cycles of ultrasonic rinsing in a 10% aqueous triton solution, acetone, and isopropanol, for 15 min each time. All the chemicals were used as received, without any further purification. The 0.5 M borate buffer (K−B_i) pH 9.2 was prepared from 0.5 M aqueous solution of H_3BO_3 (99.8%, Alfa Aesar) titrated with KOH (99%, Sigma-Aldrich) to pH 9.2. The Ni(Fe)−B_i catalysts were electrodeposited from a 0.5 mM aqueous solution of $Ni(NO_3)_2{\cdot}6H_2O$ (98.5%, Sigma-Aldrich), using 0.5 M K−B_i pH 9.2 as supporting electrolyte. The Ni(Fe)OOH catalysts were electrodeposited from a 5 mM aqueous solution of $Ni(ClO_4)_2{\cdot}6H_2O$ (Sigma-Aldrich), using KCl (≥99%, Sigma-Aldrich) with a total ionic strength of 0.1 M. The water used to prepare all solutions was deionized and ultrafiltrated by a Milipore Milli-Q system (resistivity >18.2 MΩ·cm). The electrodeposition was performed in a single compartment electrochemical cell, using an Ag/AgCl (sat. KCl, sat. AgCl) (XR300, Radiometer Analytical) as reference electrode and a coiled Pt wire as a counter electrode. All potentials are reported versus the reversible hydrogen electrode (RHE), calculated according to eq 1:

$$E^{\mathrm{RHE}} = E^{\mathrm{Ag/AgCl(sat.KCl)}} + E^{0}_{\mathrm{Ag/AgCl(sat.KCl)}} + 0.059\Delta\mathrm{pH} \qquad (1)$$

where E^{RHE} is the potential versus RHE, $E^{\mathrm{Ag/AgCl\ (sat.\ KCl)}}$ is the potential applied experimentally, and $E^{0}_{\mathrm{Ag/AgCl\ (sat.\ KCl)}}$ is the standard potential of the Ag/AgCl (sat. KCl) versus the normal hydrogen electrode (0.197 V),[27] ΔpH accounts for the difference in pH of the working solution respect to the normal hydrogen electrode (pH zero). The electrodeposition was performed with a potentiostat/galvanostat (EG&G PAR 283). The Ni-based electrocatalysts were deposited both potentiostatically and galvanostatically. The potentiostatic electrodeposition of Ni(Fe)−B_i was carried out at 1.7 V vs RHE. During the galvanostatic electrodeposition, the current was kept constant at 10/−10 μA for Ni(Fe)−B_i and Ni(Fe)OOH respectively. The electrodeposition of Ni(Fe)−B_i and Ni(Fe)OOH was performed for a period of time ensuring formation of ca. 20 monolayers of coverage. The time for Ni(Fe)OOH electrodeposition was calculated according to the real surface area of the working electrode in order to deposit 20 times 663 μC cm^{-2}, which corresponds to the charge needed to deposit one monolayer of closely packed metallic nickel from a Ni^{2+} solution (atomic radius of nickel 0.124 nm[28]). Theoretical estimation of time needed to fabricate Ni(Fe)−B_i films of desired thickness is difficult, since water oxidation reaction can readily occur at potentials facilitating Ni(Fe)−B_i deposition. Consequently, Ni(Fe)−B_i films of thicknesses comparable to Ni(Fe)OOH were electrodeposited with the aid of the in situ UV−vis setup described later in this section. Thus, a typical electrodeposition of a Ni(Fe)−B_i film was terminated when the change in the optical transmission of the sample (monitored in situ) was the same as for a Ni(Fe)OOH film held at potential equal to the one used during the Ni(Fe)−B_i deposition.

Electrochemical Performance of Ni(Fe)−B_i and Ni(Fe)OOH Thin Films on FTO. The same setup as described in the previous section was used for voltammetric measurements. Samples were examined either right after the preparation or after electrochemical conditioning. The polarization curves were obtained by cyclic voltammetry in the potential range 1.1−1.9 V vs RHE, scanning at 10 mV/s in KOH 0.1 M or K−B_i 0.5 M. The electrochemical conditioning procedure consisted of 200 voltammeric cycles between 1.25−2.0 V vs RHE, with a scan speed of 500 mV/s.

UV−vis Spectroscopy. The ultraviolet−visible (UV−vis) measurements were performed with a homemade setup. It consisted of a deuterium-halogen UV−vis lamp (Ocean Optics DH-2000-BAL), optical fibers (Ocean Optics, 200 μm fiber core diameter), a single compartment with 3-electrodes electrochemical cell, and a spectrometer (Ocean Optics, Maya 2000 Pro). All these elements were aligned together in such a way that UV−vis light was shone on the back side of a sample mounted in an electrochemical cell, and the transmission signal was collected on the other side by a spectrometer (see Figure S1). The change in transmission was recorded in situ while performing the electrochemical experiment. Cyclic voltammetry experiments were performed using the same setup as described above. The samples of Ni(Fe)−B_i and Ni(Fe)OOH mounted in this setup were scanned with cyclic potential (potential range 1.1−1.9 V vs RHE, scan rate of 10 mV/s) in KOH 0.1 M or K−B_i 0.5 M, and the change in transmission was simultaneously monitored.

Surface Enhanced Raman Experiments. The glassware was thoroughly cleaned before starting experiments by boiling in a 1:3

DOI: 10.1021/jacs.5b06814
J. Am. Chem. Soc. 2015, 137, 15112−15121

mixture of concentrated HNO_3/concentrated H_2SO_4 to remove organic contaminations after which it was boiled five times in water. The water used to clean glassware and to prepare solutions was demineralized and ultrafiltrated by a Milipore MiliQ system (resistivity >18.2 MΩ cm and TOC < 5 ppb). Electrolyte solutions were prepared with high quality chemicals, KOH (Sigma-Aldrich, semiconductor grade), H_3BO_3 (Merck, pro-analysis), $Ni(NO_3)_2{\cdot}6H_2O$ (Sigma-Aldrich, trace metals).

The experiments were performed in a confocal Raman microscope (LabRam HR, Horiba Yobin Yvon), using a 50X objective. The excitation source was an HeNe laser (633 nm). Backscattered light was filtered by an edge filter, directed to the spectrograph and to the detector. Details of the setup can be found in refs 29 and 30. The electrochemical SERS experiments were performed with a potentiostat/galvanostat (μAutolab Type III, Metrohm), using a homemade three-electrode and two compartment cell with the reference electrode separated by a Luggin capillary. The counter electrode used was a gold spiral, an Ag/AgCl (sat. KCl, sat. AgCl) was used as reference electrode and a roughened gold surface as working electrode. SERS experiments were made both in 0.1 M KOH and 0.5 M K−B_i pH 9.2.

All potentials for these experiments are reported versus the reversible hydrogen electrode (RHE) in the working pH, otherwise stated. The potentials of reference electrode versus RHE were calculated according to eq 1, and verified by measuring the equilibrium potential of a Pt wire electrode at the working solution saturated with H_2.

Prior to each measurement, the working electrode was mechanically polished to a mirror finish using alumina slurries (Buehler) with different grain sizes to 0.3 μm, rinsed with MiliQ water and sonicated in 1 M KOH during 5 min to remove all residuals of mechanical polishing. Next, the gold electrode was electrochemically polished by scanning 200 cycles of voltammetry in $HClO_4$ 0.1 M, scanning in the potential range 0−1.75 V vs RHE at 1000 mV/s. The electrode was roughened by 25 oxidation−reduction cycles (ORC) in KCl solution 0.1 M. The ORC were performed by scanning the potential from −0.30 to 1.30 V vs Ag/AgCl (sat. KCl, sat. AgCl) at 1000 mV/s and scanning the potential back at 500 mV/s. The potential was held for 30 s at the negative limit and for 1.3 s at the positive limit, this method is reported to produce a brownish surface that is SERS active.[31]

The roughened gold electrode was thoroughly rinsed with water to measure a cyclic voltammetry in the potential range 0−1.75 V vs RHE in $HClO_4$ 0.1 M at 50 mV/s. The surface area of the electrode was estimated based on the charge of the reduction peak of the gold oxide, assuming 390 $\mu C\ cm^{-2}$ for the charge for one monolayer of gold oxide.[32]

Nickel(II) hydroxide was formed on the roughened gold electrode by electrochemical oxidation of metallic nickel, which was plated galvanostatically from a $Ni(NO_3)_2{\cdot}6H_2O$ solution 5 mM, using KCl 0.1 M as a supporting electrolyte. The electrodeposition was carried out by applying cathodic currents (−10 μA) for a given time, in order to get ca. 20 monolayers of coverage.

Ni(Fe)−B_i was deposited potentiostatically on the roughened gold electrode from a $Ni(NO_3)_2{\cdot}6H_2O$ solution 0.5 mM, using 0.5 M K−B_i pH 9.2 as supporting electrolyte. The electrodeposition was carried out by applying 0.95 V vs Ag/AgCl (sat. KCl, sat. AgCl) for a period of 60 s.

X-ray Absorption Spectroscopy. In situ X-ray Absorption Near Edge Fine Structure (XANES) and Extended X-ray Absorption Fine Structure (EXAFS) measurements at the Ni K-edge (8.333 keV) were collected at the Dutch-Belgian Beamline (DUBBLE) at the European Synchrotron Radiation Facility (ESRF).[33] The energy of the X-ray beam was tuned by a double-crystal monochromator operating in fixed-exit mode using a Si(111) crystal pair. In situ XANES and EXAFS spectra of the samples were collected in fluorescence mode using a 9-element Ge detector (Ortec Inc.), whereas reference spectra of the metallic Ni foil and the Ni Oxide were collected in transmission mode using Ar/He-filled ionization chambers at ambient temperature and pressure. The EXAFS spectra, three scans per sample, were energy-calibrated, averaged and further analyzed using GNXAS.[34,35] In this approach, the local atomic arrangement around the absorbing atom is decomposed into model atomic configurations containing 2, ..., n atoms. The theoretical EXAFS signal $\chi(k)$ is given by the sum of the n-body contributions γ^2, γ^3, ..., γ^n, which take into account all the possible single and multiple scattering (MS) paths between the n atoms. The fitting of $\chi(k)$ to the experimental EXAFS signal allows to refine the relevant structural parameters of the different coordination shells; the suitability of the model is also evaluated by comparison of the experimental EXAFS signal Fourier transform (FT) with the FT of the calculated $\chi(k)$ function. The coordination numbers and the global fit parameters that were allowed to vary during the fitting procedure were the distance R(Å), Debye−Waller factor (σ^2) and the angles of the γ^n contributions which were defined according to the crystallographic structures used in the data analysis. The threshold energy E_k = 0 was defined at 8333 eV according to the Ni foil value.

Atomic Force Microscopy (AFM). AFM surface scans were performed using an NT-MDT Ntegra apparatus coupled with an NT-MDT P8 XPM controller and with an NT-MDT NSG30 cantilever mounted. Scans were taken over an area of 1 × 1 μm^2, with a 1 Hz frequency and a resolution of 512 × 512 points.

X-ray Photoelectron Spectroscopy (XPS). XPS experiment was performed using the Thermo Scientific K-alpha apparatus equipped with an Al K-alpha X-ray Source and a Flood Gun. Parameters used for the measurements were: spot size of 400 μm, pass energy of 50 eV, energy step size of 0.1 eV, dwell time of 50 ms, 20 scans in the vicinity of Ni 2p and O 1s orbitals binding energy. XPS spectra were corrected for the C peak position.

RESULTS AND DISCUSSION

Cyclic Voltammetry of Nickel(II) Hydroxide and Nickel Borate during Electrochemical Water Oxidation in Alkaline Media. The electrochemical properties of both nickel based oxygen evolution catalysts were first examined in different electrolyte media. It is important to mention that chemicals used throughout this work were not scrubbed of the Fe content. It has been shown that in rigorously iron-free environment, the onset for OER is about 1.8 V_{RHE},[23,25,26] whereas the reasonably low onset of 1.55 V_{RHE} that we observe in our case is indicative of Fe contamination.[22,23] We are therefore certain that a non-negligible content of Fe was unintentionally incorporated into our materials. Thus, given the enormous effect of iron impurities on activity of Ni-based OECs toward OER, the studied compounds should be considered as Ni(Fe)OOH and Ni(Fe)−B_i and not as NiOOH and Ni−B_i.

Figure 1 shows the cyclic voltammetry of nickel(II) hydroxide in 0.1 M KOH pH 13 (dotted black line). The pair of peaks in the potential region 1.25−1.50 V vs RHE is attributed to the Ni^{2+}/Ni^{3+} redox couple,[36,37] followed by the

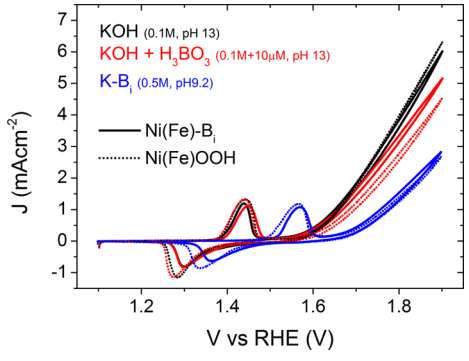

Figure 1. Polarization curves of Ni(Fe)−B_i (solid lines) and Ni(Fe)OOH (dotted lines) in 0.1 M KOH (black) 0.1 M KOH + 0.01 M H_3BO_3 (red) and 0.5 M K−B_i (blue). Scan rate: 10 mV/s.

DOI: 10.1021/jacs.5b06814
J. Am. Chem. Soc. 2015, 137, 15112−15121

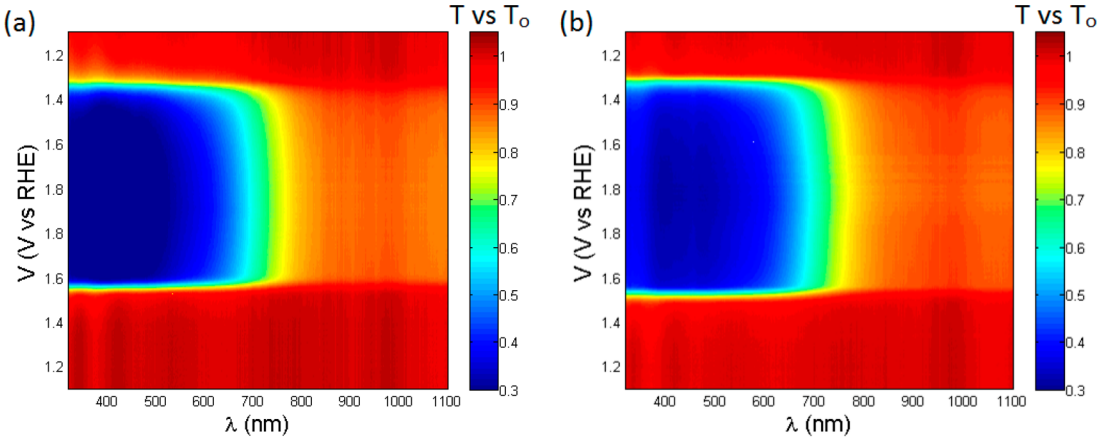

Figure 2. Contour plots of normalized transmission as a function of wavelength and potential for (a) Ni(Fe)−B_i and (b) Ni(Fe)OOH in 0.5 M K−B_i electrolyte, pH 9.2.

electrochemical oxygen evolution at potentials higher than 1.6 V vs RHE.

$Ni(OH)_2$ is reported to crystallize in a disordered α-$Ni(OH)_2$ phase, that oxidizes to form γ-NiOOH at ca. 1.35 V vs RHE.[36,37] The α/γ transition correspond to the Ni^{2+}/Ni^{3+} redox couple of the nickel-based catalyst and will be referred as the α/γ transition in the rest of the work. The potential region for the α/γ transition measured in this work corresponds well with the previously reported data.[24,36] The catalytic activity of $Ni(Fe)(OH)_2$ was also studied in a borate buffer electrolyte held at pH 9.2 in order to understand the effect of the borate anion on the catalytic activity of the hydroxide toward the oxygen evolution reaction. The study of the electrocatalytic activity of $Ni(Fe)(OH)_2$ in borate media allows us to get a better understanding of the catalytic activity measured for Ni(Fe)−B_i, which will be presented later. From the cyclic voltammetry of a sample of $Ni(Fe)(OH)_2$ in borate buffer pH 9.2 (Figure 1, dotted blue line) is noticeable that the potential for the $Ni(OH)_2$/NiOOH transition shifts to higher potentials by about 0.1 V, and the activity toward oxygen evolution is seriously inhibited when compared with the activity observed in KOH.

We also investigated the electrochemical properties of $Ni(Fe)(OH)_2$ in KOH with the slight addition of H_3BO_3 (Figure 1, dotted red line) to test if the borate anions are the cause of the observed inhibitory effect in K−B_i. Boric acid was added to KOH 0.1 M to give a nominal H_3BO_3 concentration of 0.01 M. The pH of this solution was approximately 12.5, which is very close to the pH 13 of pure KOH 0.1 M, so we can neglect the pH effect. The results indicate that at pH 13 the borate anion does not influence the catalytic activity of $Ni(Fe)(OH)_2$ toward water oxidation, but the enhanced activity is rather related to the effect of the electrolyte pH.

The catalytic activity toward oxygen evolution was also studied for Ni(Fe)−B_i. The cyclic voltammetry of nickel borate in KOH (Figure 1, solid black line) shows the typical α/γ transition in the potential region 1.25−1.50 V vs RHE, similar to the region where the transition occurs in nickel(II) hydroxide. The current density for oxygen evolution in KOH 0.1 M catalyzed by Ni(Fe)−B_i is similar to the values obtained for the reaction catalyzed by $Ni(Fe)(OH)_2$. Ni(Fe)−B_i was also tested in borate buffer pH 9.2, and the results of cyclic voltammetry are shown in Figure 1 (solid blue line). The results look quite similar to the voltammogram of $Ni(Fe)(OH)_2$ in the same media. Again, the α/γ transition shifts to more positive potentials and the current density associated with oxygen evolution is lower than the one observed in 0.1 M KOH. Importantly, no significant differences in the electrochemical characteristics of the two studied OECs were observed.

To further decouple the role of pH and borate concentration in the inhibitory effect of K−B_i pH 9.2, we tested Ni(Fe)OOH in electrolyte with a fixed borate concentration of 0.5 M while changing the amount of KOH to control the pH in the range 9.2−13. We decided to release the restraint of constant total ionic concentration and not use any supporting electrolyte in order to avoid specific adsorption of other anions that could drastically change the chemistry at the solid/liquid interface and hence mask the effect of the borate anions. The results are presented in Figure S2 as JV curves. The cyclic voltammetries obtained in the pH range 9.2−10 clearly show higher OER-related Tafel slopes than for measurements performed above pH 11. The Tafel slopes in pH 11−13 are quite the same as in 0.1 M KOH pH 13 (the small differences observed can be attributed to the difference in ionic strength). The data in Figure S2 clearly show that borate hinders the catalytic activity below pH 10, results that agree well with the kinetic study reported by Bediako et al.[20] In addition to that, we have shown that borate anions do not affect the OER catalytic activity of Ni(Fe)OOH at highly alkaline pHs (above pH 11).

In Situ Electrochemical UV−vis Spectroscopy of Nickel(II) Hydroxide and Nickel Borate during Electrochemical Water Oxidation in Alkaline Media. To further confirm the structural changes in our catalysts during voltammetric cycling, a UV−vis study was performed. The results obtained by UV−vis spectroscopy are summarized in Figure 2a,b as contour plots of the normalized transmission (T/T_0) as a function of wavelength and potential, obtained during cycling voltammetric experiments on Ni(Fe)−B_i (Figure 2a) and Ni(Fe)OOH (Figure 2b) catalyst.

The transmission values for a number of selected wavelengths were plotted against the electrode potential, and they are shown with the corresponding polarization curves in Figure S3a-b for Ni(Fe)−B_i and Ni(Fe)OOH catalysts.

During the anodic voltammetric sweep, the transmission of Ni(Fe)OOH drops very sharply, down to about 35% of the initial value. When scanning back in the negative direction, we record an opposite change as the transmission increases. These

DOI: 10.1021/jacs.5b06814
J. Am. Chem. Soc. 2015, 137, 15112−15121

optical transitions occur reversibly, i.e., during cathodic sweeps the optical properties are reverted back to the initial state at the end of each voltammetric cycle. Interestingly, the potentials at which the optical transitions occur coincide very well with the potentials at which the oxidation and reduction waves are observed (Figure S3). When scanning anodically, at potentials corresponding to the onset of the Ni^{2+}/Ni^{3+} oxidation wave (ca. 1.5 V vs RHE), the transmission starts to decrease. The end of the transition coincides well with the offset of the Ni^{2+}/Ni^{3+} oxidation wave (ca. 1.6 V vs RHE). In the OER potential regime, the transmission remains relatively unchanged. During a cathodic sweep, a reverse optical transition can be observed in between potentials corresponding to the Ni^{3+}/Ni^{2+} reduction wave onset and offset (ca. 1.4 and 1.25 V vs RHE). Importantly, these redox waves correspond to the catalyst activation. These results imply that significant light absorption by these OECs is inherent to the catalytically active state.

Corrigan et al. have performed an extensive study of electrochromism in thin films of NiO_x and $Ni(OH)_2$.[38−41] They showed huge differences in optical properties of NiO_x films subjected to various potentials: initially transparent NiO_x attains brownish color upon oxidation. Our results are in agreement with their findings. Furthermore, results from the group of Lampert[42] show that coloring of $Ni(OH)_2$ occurs more rapidly than bleaching of NiOOH. This is consistent with our results, i.e., the potential window at which the optical transition occurs is more narrow in case of the anodic sweep than the cathodic one, resulting in a steeper slope of the transmission versus potential hysteresis. Likewise, the oxidation wave itself is narrower than the reduction one. Our results are also in agreement with a recent report from the Boettcher group,[43] which has shown that in situ spectrophotometry can be successfully applied to study electrochromic effects in OECs undergoing redox reactions.

The spectral characteristics of the observed optical transition in Figure 2 are dominated by a strong and broad absorption feature observed for wavelengths below 800 nm. This feature may correspond to a nickel d−d interband transition. Importantly, no significant differences between Ni(Fe)−B_i and Ni(Fe)OOH were observed in our UV−vis spectral investigation, in agreement with our electrochemical study which did not show major differences between Ni(Fe)−B_i and Ni(Fe)OOH (as shown in Figure 1).

In Situ Surface Enhanced Raman Spectroscopy (SERS) of Nickel(II) Hydroxide and Nickel Borate during Electrochemical Water Oxidation in Alkaline Media. The Raman spectra of the $Ni(Fe)(OH)_2$ in KOH 0.1 M, measured in the potential region 1.0−1.9 V vs RHE are shown in Figure 3a. The spectra in the potential region previous to the nickel oxidation (1.0−1.3 V vs RHE) show two peaks at ca. 450 and 500 cm^{-1}. Those peaks have been assigned to A_{1g} stretching modes of Ni—OH and Ni−O, respectively.[37,44−48] The alpha phase of nickel hydroxide is a hydrated compound that would easily deprotonate by applying anodic potentials,[44] this deprotonation effect explains the evolution of the peak at ca. 500 cm^{-1} when the applied potential becomes more positive.

When the applied potential is higher than 1.4 V vs RHE, the α/γ transition takes place, and the Raman spectra shows two peaks at ca. 479 and 562 cm^{-1}. These peaks match well with the e_g bending vibration and the A_{1g} stretching vibration of Ni−O in γ-NiOOH.[36,37,44,47] Furthermore, Figure 3a shows that the Raman spectra develop rather broad peaks in the region ca.

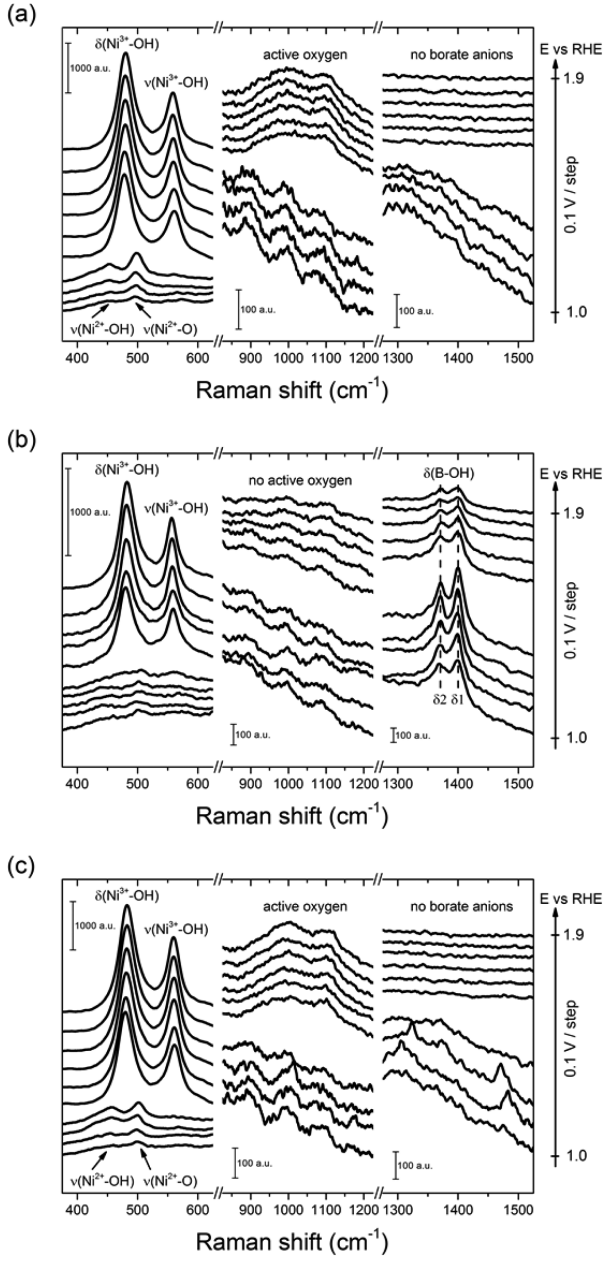

Figure 3. SER spectra of freshly prepared $Ni(Fe)(OH)_2$ acquired in the potential range 1.0−1.9 V vs RHE in (a) 0.1 M KOH pH 13, (b) 0.5 M K−B_i pH 9.2, and (c) 0.1 M KOH + 0.01 M H_3BO_3. The measurements were performed potentiostatically.

900−1150 cm^{-1} when the γ-NiOOH is formed. Merril and co-workers[48] reported the same signals during the charge−discharge process of $Ni(OH)_2$ in concentrated KOH and attribute the signal to formation of "active oxygen" on the surface of the charged nickel hydroxide (NiOOH), they also described this species as "O^0". The question that rises around this signal is what is the nature of that activated oxygen and how does it relate with the OER activity. The SERS study in moderately alkaline pH (pH 9.2) provides evidence to address that question and lead to conclusions about its effect on the OER activity.

Figure 3b shows the Raman spectra of $Ni(Fe)(OH)_2$ in 0.5 M K−B_i at pH 9.2 obtained in the potential region 1.0−1.9 V vs RHE. The wavenumber region 400−600 cm^{-1} looks similar to the one observed in KOH 0.1 M that is two

DOI: 10.1021/jacs.5b06814
J. Am. Chem. Soc. 2015, 137, 15112−15121

peaks that can be assigned to the A_{1g} stretching modes of Ni−OH and Ni−O (see Figure 3a). The main difference that can be observed is the delay in the appearance of the intense peaks at ca. 479 and 562 cm^{-1}. These peaks now appear at potentials higher than 1.5 V vs RHE which is in agreement with the results obtained from the cyclic voltammetry, where it can be seen that the α/γ transition occurs at higher potentials in 0.5 M K−B_i pH 9.2 when compared with the results in 0.1 M KOH (see Figure 1). Furthermore, the Raman spectra of Ni(Fe)$(OH)_2$ collected in K−B_i differs substantially from the signals observed in KOH in the wavenumber region 800−1500 cm^{-1}. There are no peaks in the region 900−1150 cm^{-1}, which suggests that the formation of "active oxygen O^0" during α/γ transition is somehow hindered in K−B_i pH 9.2. Additionally, the spectra acquired in borate buffer show two peaks at ca. 1370 and 1400 cm^{-1} that can be assigned to the in-plane bending vibration of the B−OH in $[B(OH)_4]^-$ ions present in the buffer solution.[49,50]

The spectra in Figure 3a show the formation of the "active oxygen" species, similar to the results reported in literature.[48] However, there are no Raman peaks corresponding to this species when freshly prepared Ni(Fe)$(OH)_2$ is oxidized in K−B_i pH 9.2 (Figure 3b), which indicates that the formation of this "O^0" species strongly depends on the electrolyte pH. Furthermore, the catalytic activity of Ni(Fe)$(OH)_2$ for OER is higher in 0.1 M KOH than in 0.5 M K−B_i pH 9.2 (see Figure 1) so one might wonder whether the generation of "active oxygen" sites in the Ni(Fe)OOH enhances its OER activity.

To address the effect of the borate anions on the generation of the "active oxygen" species, we also collected Raman spectra of Ni(Fe)$(OH)_2$ in 0.1 M KOH spiked with boric acid to give a nominal H_3BO_3 concentration of 0.01 M (Figure 3c), the pH of this solution if approximately 12.5 so close to the pH 13 of pure 0.1 M KOH thus isolating the role of the borate anions. The spectra in Figure 3c show the Raman peaks at ca. 479 and 562 cm^{-1}, assigned to the $\delta(Ni^{3+}-OH)$ and $\nu(Ni^{3+}-OH)$ modes, respectively. Those peaks appear above 1.4 V vs RHE, similar to the peaks observed in 0.1 M KOH (see Figure 3a). Most interestingly, the oxidized Ni(Fe)OOH shows the peaks between 900−1150 cm^{-1}, which are assigned to "active oxygen". The spectra in Figure 3c provides clear evidence that the borate anions do not play an inhibitory role in the formation of the "active oxygen" at pH 13, and therefore they do not affect the OER activity of the Ni(Fe)OOH catalyst at pH 13.

Our spectroelectrochemical results are consistent with the kinetic data reported by Nocera and co-workers, where they demonstrated that borate anions have an inhibitory effect on the OER activity of a nickel-based catalyst (Ni−B_i) at pH 9.2.[20] Furthermore, we now present results that suggest the lack of inhibitory effect of borate anions on the OER activity of nickel-based catalysts at pH 13. It is important to consider that the isoelectric point of nickel(II) hydroxide lies in the pH range 10−11,[51] thus the NiOOH catalyst is expected to be negatively charged at pH 13 and the adsorption of the borate anions to be hindered. It is consistent with results shown in Figure S2, where a distinct change in the Tafel slope in the pH range 10−11 can be observed. Moreover, the inhibitory effect of borate anions at pH 9.2 can be observed in our electrochemical results (see Figure 1) and further verified with the spectroscopic data in Figure 3b, where one can see that the formation of the OER active Ni(Fe)OOH is delayed in borate buffer. Furthermore, Ni(Fe)$(OH)_2$ does not seem to oxidize in the buffer electrolyte until the borate anions are depleted from the surface as it is shown in the plot of the integrals of the $\delta(Ni^{3+}-OH)$, $\nu(Ni^{3+}-OH)$ and $\delta(B-OH)$ peaks in Figure S4a.

Figure 4a shows the Raman spectra of Ni(Fe)−B_i in 0.1 M KOH pH 13 obtained in the potential region of

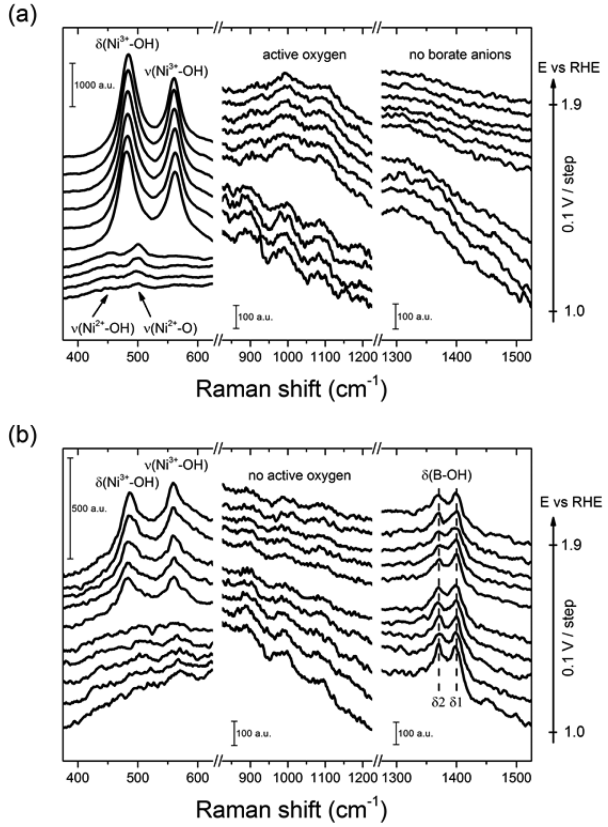

Figure 4. SER spectra of freshly prepared Ni(Fe)−B_i acquired in the potential range 1.0−1.9 V vs RHE in (a) 0.1 M KOH pH 13 and (b) 0.5 M K−B_i pH 9.2. The measurements were performed potentiostatically.

1.0−1.9 V vs RHE. The spectra show that Ni(Fe)−B_i oxidizes to form a oxyhydroxide with similar features to the ones observed in the Raman spectra of Ni(Fe)$(OH)_2$/Ni(Fe)OOH (see Figure 3a). The SER spectra of Ni(Fe)−B_i show the two peaks at 479 and 562 cm^{-1} corresponding to the bending and stretching modes of Ni^{3+}−OH respectively, and the broad peaks in the region ca. 900−1150 cm^{-1} attributed to the formation of the "active oxygen" species. Noteworthily, the peaks at ca. 1370 and 1400 cm^{-1} attributed to the B−OH bending modes of the $[B(OH)_4]^-$ anions are not present in Figure 4a. This shows that there are no borate ions bonded to the catalyst in the "nickel borate" compound, which seems to deposit as form of Ni$(OH)_2$ that gets oxidized to NiOOH. This statement can be also confirmed by looking at the stretching modes of Ni^{2+}−O in the potential region 1.0−1.3 V vs RHE (see Figure 4a).

SER spectra of Ni(Fe)−B_i obtained during the electrochemical water oxidation in K−B_i (see Figure 4b) resemble the same features observed for the spectra of Ni(Fe)$(OH)_2$ in K−B_i: two peaks at ca. 480 and 557 cm^{-1} appear at potentials above 1.5 V vs RHE, which correspond to formation of nickel oxyhydroxide. Likewise, we observe a pair of peaks at 1370 and 1400 cm^{-1}, which can be assigned to the borate ions bonded to

DOI: 10.1021/jacs.5b06814
J. Am. Chem. Soc. 2015, 137, 15112−15121

the catalyst. Again, the peaks in the wavenumber region of 900−1150 cm^{-1} are absent, suggesting that in K−B_i pH 9.2, the formation of the "active oxygen" species is hindered, which explain the lacks of activity observed in the cyclic voltammetry in Figure 1. This also supports our hypothesis about the role of the "active oxygen" for the OER electrocatalysis. Furthermore, the spectra in Figure 4b shows that the borate anions are adsorbed on the Ni(Fe)−B_i catalyst but they need to get depleted in order to form the OER active NiOOH-like catalyst. This can be further verified by looking at the integral of the $\delta(Ni^{3+}-OH)$, $\nu(Ni^{3+}-OH)$, and $\delta(B-OH)$ peaks in Figure S4b. From that figure, it is clear that the formation of the OER active NiOOH-like form of the catalyst (indicated by increase of the integral of $\delta(Ni^{3+}-OH)$, $\nu(Ni^{3+}-OH)$ peaks) occurs with the concomitant depletion of the borate anions (indicated by diminishing of the integral of the $\delta(B-OH)$ peak). The spectroelectrochemical evidence show that borate anions do also absorb on the Ni(Fe)−B_i catalysts at pH 9.2 and act as inhibitors of the OER activity of the catalyst, which is in full agreement with the kinetic data previously reported by Nocera and co-workers.[20]

Regarding the nature of the "active oxygen" species, Merril and co-workers did not specify the chemical nature of it, neither did our spectroelectrochemical data allow us to unequivocally identify it. However, experimental and DFT data have shown that nickel peroxide and nickel superoxide have vibrational modes in the wavenumber region 900−1150 cm^{-2}.[52−54] These reports lead us to think that this "active oxygen" species may have peroxidic or superoxidic nature. Furthermore, the strong pH-dependency of the Raman peak associated with this species indicate that the "active oxygen" is actually formed via deprotonation of the nickel oxyhydroxide to produce a negatively charge nickel oxide ($NiOO^-$).

Manganese oxide has also been reported to deprotonate in a process that is strongly dependent on the electrolyte pH, and this deprotonation influences the activity of the oxide toward oxygen evolution.[55]The authors propose that the deprotonation of $Mn^{3+}-OH$ sites toward negatively charged $Mn^{3+}-O^-$ is responsible for the activity enhancement. These findings are in full agreement with pH effect on the OER activity reported in this work. We therefore propose that formation of the "active oxygen" species occurs via a deprotonation of nickel oxyhydroxide that produces negatively charged sites on the surface of the nickel oxyhydroxide (with peroxidic or superoxidic nature). This species acts as a precursor for oxygen production in a similar manner as the one reported for manganese oxide.

Looking at the big picture, we believe that "active oxygen" can be regarded as a preferential active site for water oxidation. We speculate that it facilitates a more favorable (i.e., requiring less overpotential) pathway for water oxidation. However, when the Ni centers are already in the higher valency state and accordingly the "active oxygen" species are present at the surface, once an even more positive bias voltage is applied, the reaction kinetics improve and the reaction proceeds faster and with a higher efficiency, as seen by a typical exponential trend of the current density. However, the number of active sites, and thus the signal from the active oxygen, seem not to scale with potential because the formation of this "active" structure that facilitates the enhanced OER catalysis occurs entirely during the nickel oxidation reaction. Therefore, the Raman signal stays unchanged even at highly oxidative potentials (Figure 3a−c and Figure 4a). This implies that we are not creating any more active sites at higher potentials, but we are just driving them with more potential and thereby increasing the kinetics of the OER. This is in agreement with our experimental findings; the Raman features related to active oxygen appear only in the spectra collected for samples that show a low onset in the CV data (Figure 1, black and red curves). On the other hand, with the samples that do not show the active oxygen feature (both catalysts at pH 9.2), the onset for the OER is larger, and the Tafel slope is increased compared to the samples tested at higher pH. This shows that the formation of the active oxygen species, which is favorable for efficient water oxidation, occurs only in strong alkaline media, and thus there is a clear structure/functionality relationship between the catalyst and the electrolyte in which it is tested. In other words, we do not regard the formation of active oxygen species as something inherent to the catalyst alone (presumably a catalyst showing high activity) but rather as something that can be triggered by appropriate coupling of the catalyst and the electrolyte, to result in high overall OER activity.

The similarities between the Ni(Fe)OOH and Ni(Fe)−B_i catalyst in the catalytically active state were also confirmed by X-ray photoelectron spectroscopy (XPS) (see Figure S5), the pristine nickel oxyhydroxide and nickel-borate catalysts exhibit small differences in the Ni 2p and O 1s binding energies, but those differences disappear when the catalysts are subjected to electrochemical conditioning, after which the XPS spectra are virtually the same, indicating that the chemical state of both electrochemically conditioned catalysts is quite similar.

The microstructure was also verified, using Atomic Force Microscopy (AFM) (see Figure S6), the grain size was comparable for both electrocatalysts, although the distribution of the grains is different. The Ni(Fe)−B_i catalyst deposits in an arrangement of closely packed nanoclusters, whereas the Ni(Fe)OOH compound deposits in a rather chaotic network, without any apparent higher-order structure.

It has recently been reported[23,25,26] that iron impurities present in the electrolyte can improve the electrocatalytic activity toward oxygen evolution of NiOOH. Therefore, the question arises whether those impurities might affect the effect of pH on the activity, as presented in this work. The chemicals used during electrodeposition, anodization and cyclic voltammetry were not scrubbed of Fe content, therefore our OEC films can be expected to contain considerable amounts of Fe.[22,23] The KOH and H_3BO_3 used in this work were reagent grade chemicals with Fe content <1 ppm, and they were not purified according the method of Trotochaud et al.,[23] so we expect that Fe is present in our films. Both KOH and H_3BO_3 used have a similar content of Fe but the measured catalytic activity at pH 9.2 is approximately twice as low at pH 13. This shows that the catalyst deprotonation toward formation of activated oxygen species has a real effect on the catalytic activity, which is not related with the Fe impurities in the electrolyte. We further proved this statement by measuring the catalytic activity toward oxygen evolution on NiFe double hydroxide (50% Fe) in KOH 0.1 M (pH 13) and in phosphate buffer pH 7 (see Figure S7). The results of this experiment clearly show that even in the presence of iron, the catalytic activity of Ni(Fe)OOH at pH 7 is negligible, so the deprotonating effect of the alkaline electrolyte plays crucial role for the enhanced catalytic activity toward electrochemical oxygen evolution normally observed in Ni-based catalysts in alkaline media.

It is important to mention that we are not disregarding the effect of Fe impurities in the electrolyte, which is reported to

DOI: 10.1021/jacs.5b06814
J. Am. Chem. Soc. 2015, 137, 15112−15121

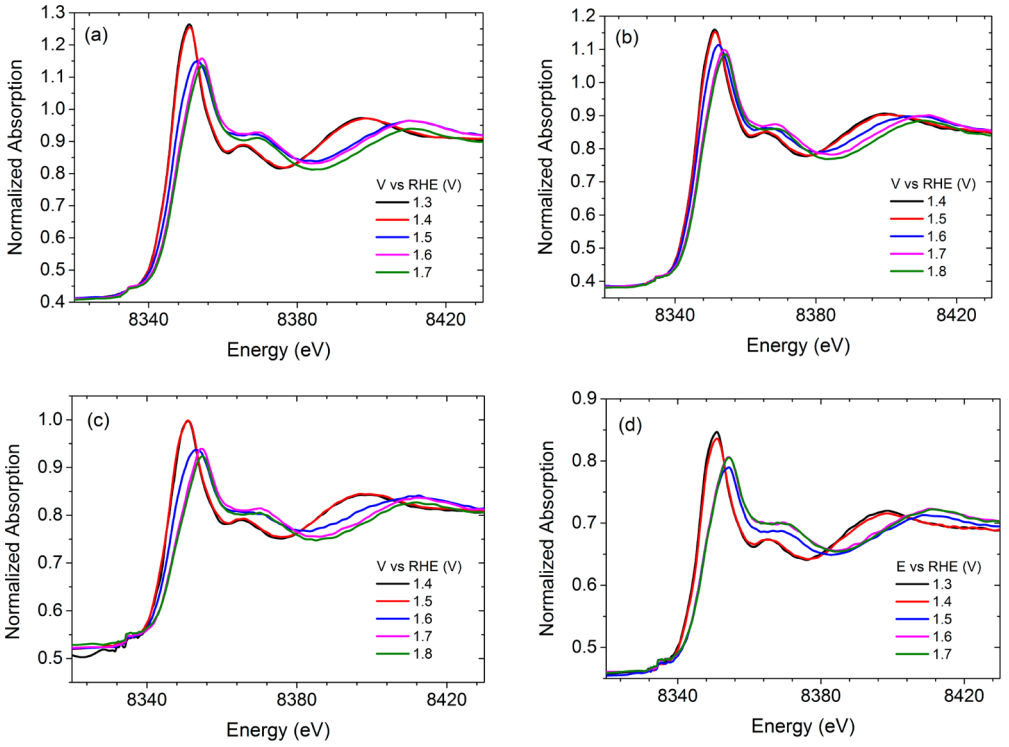

Figure 5. In situ Ni K-edge XAS spectra acquired during potentiostatic OER experiments on anodized Ni(Fe)OOH and Ni(Fe)−B_i electrocatalysts deposited on FTO. (a) XANES spectra of Ni(Fe)OOH during OER in 0.1 M KOH. (b) XANES spectra of Ni(Fe)OOH during OER in borate buffer pH 9.2. (c) XANES spectra of Ni(Fe)−B_i during OER in 0.1 M KOH. (d) XANES spectra of Ni(Fe)−B_i during OER in borate buffer pH 9.2.

enhance the activity of Ni-based OECs. We acknowledge that the presence of iron is absolutely crucial for efficient OER and it is very well possible that iron is the active site for OER in Ni-based OECs. Nevertheless, in our report, we analyze the activity of Ni-based catalysts regardless of Fe content. We focus on coupling of Ni-based OECs with the electrolyte and specifically consider the role of pH and borate concentration. Our evidence shows that the deprotonating effect of hydroxyl anions to form highly oxidized nickel sites in the catalyst also plays a very important role to reach high catalytic activity, and needs to be carefully considered in the development of nickel-based catalysts for the oxygen evolution reaction at moderate pHs. We show that the formation of the active oxygen species is an additional mechanism that can give rise to an even higher OER activity than based on the Fe impurities alone. The formation of the active oxygen species is facilitated by alkaline conditions and seems to be independent of the Fe content in NiOOH, i.e., regardless of the exact composition of the catalyst, the active oxygen species can promote higher OER activity. We are confident to ascribe this effect to the electrolyte properties and not the Fe-impurities, since similar observations have been made for Fe-free systems.[56]

In Situ X-ray Absorption Spectroscopy Measurements of Nickel(II) Hydroxide and Nickel Borate during Electrochemical Water Oxidation in Alkaline Media. Figure 5a−d shows the in situ X-ray Absorption Near Edge Fine Structure (XANES) spectra as a function of the applied potential, acquired during potentiostatic experiments for oxygen evolution on Ni(Fe)OOH and Ni(Fe)−B_i electrocatalysts, in KOH 0.1 M and borate buffer pH 9.2. The edge position in the all XANES spectra shift to higher energies when the electrode potential becomes more positive, which is consistent with the fact that the nickel sites of $Ni(Fe)(OH)_2$ and Ni(Fe)−B_i oxidizes at potentials higher than ca. 1.4 V vs RHE (KOH 0.1 M) and 1.5 V vs RHE (borate buffer pH 9.2), as it can be seen in the voltammetries of Figure 1. According to literature data,[21,57] the increase in the oxidation state of nickel in NiOOH induces changes in its local chemical environment, and consequently a crystallographic phase changing from trigonal/rhombohedral to monoclinic occurs.

Interestingly, XANES spectra of both OECs, anodized Ni(Fe)OOH and Ni(Fe)−B_i collected at various applied potentials look very similar (Figure 5a,b in comparison with Figure 5c,d), this supports the idea that the nickel−borate catalyst in its active state is a form of γ-NiOOH, which is in agreement with the voltammetric and spectroscopic evidence presented in the previous sections. Our results are in agreement with some other XAS studies available in the literature.[21,58] The work of Bediako et al.[21] shows that anodized Ni−B_i is very similar to γ-NiOOH in terms of the XANES edge position, formal nickel oxidation state, and the EXAFS spectra. Likewise, we find virtually no differences between Ni(Fe)−B_i and Ni(Fe)OOH.

The local environment analysis of Ni catalyst samples was achieved by performing Extended X-ray Absorption Fine Structure (EXAFS) measurements at the Ni K-edge (see Figures S9 and S10). The experimental data were analyzed according to GNXAS approach which allowed us to construct the signal corresponding to the molecule from known scattering amplitudes and phases. In this way, the structural signal was constructed entirely ab initio and then fitted to the experimental data. To generate the theoretical signals needed to fit the data, the β-NiOOH and γ-NiOOH (swollen phase) crystallographic phase were used.[21,57] These compounds have, respectively, a trigonal/rhombohedral and monoclinic crystal structure.

DOI: 10.1021/jacs.5b06814
J. Am. Chem. Soc. 2015, 137, 15112−15121

The space group that describe the structure of β-NiOOH is $P\bar{3}m1$, with the following unit cell parameters: $a = b = 3.1170$ Å , $c = 4.595$ Å, $\alpha = \beta = 90°$, $\gamma = 120°$. The space group used to describe the γ-NiOOH phase is $C2/m$, with the following unit cell parameters: $a = b = 2.8295$ Å, $c = 20.9472$ Å, $\alpha = \beta = 90°$, $\gamma = 119.74°$.

The Ni atoms in both cases coordinate six oxygen atoms but in the β-NiOOH, due to the Jahn–Teller effect, there is a strongly distorted octahedral geometry caused by the elongation of the Ni–O distance along the axial direction.[21] The low symmetry of this structure results in two different Ni–O distances being detected in β-NiOOH (Ni–O equatorial: 1.87 Å and Ni–O axial: at 2.03 Å), but the limited k range measured makes it impossible to gather these data. This allows the ability to keep the model as simple as possible and to reduce the numbers of fitting parameters. With this approximation, the local environment of the Ni can be modeled by using two two-body γ_2^1 and γ_2^2 signals representing the Ni–O and Ni–Ni distances, respectively.

The γ-NiOOH structure was modeled with periodically alternating repetitions of edge-shared octahedra arranged into higher ordered layers, which are interstratified with alkali cations and water molecules, which is in agreement with the report from Risch et al. proposes that the structure of Ni–B_i may be composed of fragments of layered γ-NiOOH separated by water and borate molecules.[58] This approximation makes the model simple and allows us to reduce the numbers of fitting parameters. In this model, the Ni local environment can be simulated by using two two-body γ_2^1, γ_2^2, and two three body signals γ_3^1 and γ_3^2.

In Figure 6, representing a sketch of a swollen phase, the γ_2^1 is relative to the Ni–O distance at 1.985 Å, γ_2^2 is the Ni–O at 2.77 Å. The three body configurations γ_3^1 and γ_3^2, the γ_3^1 is relative to the Ni–O–Ni triangular arrangements with $\theta \approx 140°$ and having a long Ni–Ni distance at 5.00 Å, whereas γ_3^2 takes into account the collinear configuration with θ 180°, having the Ni–Ni distance at 5.65 Å. In this configuration, the only free parameter is the angle. The distances, the Debye–Waller factors, and the coordination numbers are directly linked by geometrical consideration to the first two shells. It is worth mentioning that the coordination numbers for these distances in the ideal structure are equal to six. The fitting results obtained on the samples are reported in Tables S1 and S2 and shown in Figure 6.

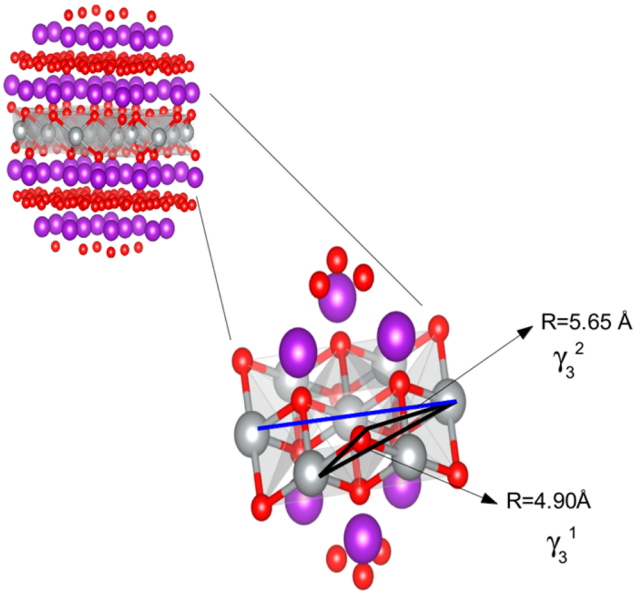

Figure 6. Sketch of the swollen γ-NiOOH phase. For sake of clarity, the direct Ni–O and Ni–Ni distance are not shown but only the two three-body configurations are evidenced in black and in blue lines.

CONCLUSIONS

We have presented a systematic spectroelectrochemical study of the electrocatalytic activity toward oxygen evolution of two Ni-based OECs (Ni(Fe)–B_i and Ni(Fe)OOH). The recorded broad SERS peaks in the region ca. 900–1150 cm^{-1} clearly show that Ni(Fe)–B_i and Ni(Fe)OOH get charged prior the actual OER, and those negatively charged sites in the OECs act as OER precursors. We propose that the formation of those "active oxygen" sites occurs via a deprotonation process that strongly depends on the pH of the electrolyte. The chemical identity of the "active oxygen" species is still unclear but its Raman peak appears in the region that nickel peroxide and superoxide have vibrational modes, suggesting that the species may have peroxidic or superoxidic nature. It is noteworthy that the effect of the deprotonation process is crucial at moderate pHs, as even Fe-doped Ni-based catalysts shows negligible activity in neutral pH 7. These results clearly demonstrate that the deprotonating effect in strongly alkaline electrolytes has an important effect on the catalytic activity of nickel-based compounds and should be carefully considered in addition to the Fe content if one would like to develop Ni-based electrocatalysts meant to catalyze the OER at moderate pHs.

The SERS, UV–vis, and XAS evidence collected in this work suggest that α-$Ni(OH)_2$ and Ni–B_i get activated through the formation of very similar oxyhydroxide species. Furthermore, Ni(Fe)–B_i and Ni(Fe)OOH show similar electrochemical characteristics in a given electrolyte, i.e., similar OER electrocatalytic activity and electrolyte dependence. We could not find any evidence for the importance of the boron presence in the structure of Ni(Fe)–B_i. Therefore, we conclude that in the active state, Ni(Fe)–B_i and Ni(Fe)OOH are chemically the same, namely forms of NiOOH.

Furthermore, the in situ UV–Vis spectroscopic study of Ni(Fe)–B_i and Ni(Fe)OOH showed that both OECs absorb a huge portion of light in the catalytically active state. This needs to be taken into consideration when applying this sort of catalyst on photoelectrochemical devices.

Our work has clearly shown that a catalyst should not be studied separately from its environment; in Ni-based OECs, the phase-nature and activity of the catalyst is strongly dependent on the electrolyte properties, and therefore, such a system should be studied as a whole.

ASSOCIATED CONTENT

Supporting Information

The Supporting Information is available free of charge on the ACS Publications website at DOI: 10.1021/jacs.5b06814.

Figure S1, Schematic view of the electrochemical setup; Figure S2, JV curves of Ni(Fe)OOH; Figure S3, transmission vs potential curves for a number of selected wavelengths and the corresponding polarization curves; Figure S4, evolution of the integral of the Ni–O and B–OH Raman peaks; Figure S5, collected XPS spectra; Figure S6, AFM Scans; Figure S7, polarization curve for

DOI: 10.1021/jacs.5b06814
J. Am. Chem. Soc. 2015, 137, 15112–15121

oxygen evolution; Figure S8, SER spectra of the gold electrode; Figure S9, EXAFS results obtained during the electrochemical water oxidation in Ni(Fe)OOH; Figure S10, EXAFS results obtained; Tables S1 and S2, fitting parameters of the EXAFS spectra; and additional references (PDF)

AUTHOR INFORMATION

Corresponding Author

*W.Smith@tudelft.nl

Author Contributions

‖These authors contributed equally to this work

Notes

The authors declare no competing financial interest.

ACKNOWLEDGMENTS

This research is financed in part (B.J.T., O.D-M., M.T.M.K., and W.A.S) by the BioSolar Cells open innovation consortium, supported by the Dutch Ministry of Economic Affairs, Agriculture and Innovation. A.L. and W.B. acknowledge The Netherlands Organisation for Scientific Research (NWO) for financial support. Helpful discussions with Fatwa Firdaus Abdi and Wim Haije in the initial phase of this work are greatly acknowledged.

REFERENCES

(1) Hermans, J. *Energy Survival Guide*; Leiden University Press: Leiden, 2011; pp 65−164.
(2) Hoffert, M. I.; Caldeira, K.; Jain, A. K.; Haites, E. F.; Harvey, L. D. D.; Potter, S. D.; Schlesinger, M. E.; Schneider, S. H.; Watts, R. G.; Wigley, T. M. L.; Wuebbles, D. J. *Nature* **1998**, *395*, 881.
(3) Lewis, N. S.; Nocera, D. G. *Proc. Natl. Acad. Sci. U. S. A.* **2006**, *103*, 15729.
(4) Crabtree, G. W.; Dresselhaus, M. S.; Buchanan, M. V. *Phys. Today* **2004**, *57*, 39.
(5) Koper, M. T. M. *J. Electroanal. Chem.* **2011**, *660*, 254.
(6) Man, I. C.; Su, H.-Y.; Calle-Vallejo, F.; Hansen, H. a.; Martínez, J. I.; Inoglu, N. G.; Kitchin, J.; Jaramillo, T. F.; Nørskov, J. K.; Rossmeisl, J. *ChemCatChem* **2011**, *3*, 1159.
(7) Matsumoto, Y.; Sato, E. *Mater. Chem. Phys.* **1986**, *14*, 397.
(8) Gong, M.; Dai, H. *Nano Res.* **2015**, *8*, 23.
(9) Gong, M.; Li, Y.; Wang, H.; Liang, Y.; Wu, J. Z.; Zhou, J.; Wang, J.; Regier, T.; Wei, F.; Dai, H. *J. Am. Chem. Soc.* **2013**, *135*, 8452.
(10) Lu, Z.; Xu, W.; Zhu, W.; Yang, Q.; Lei, X.; Liu, J.; Li, Y.; Sun, X.; Duan, X. *Chem. Commun.* **2014**, *50*, 6479.
(11) Song, F.; Hu, X. *Nat. Commun.* **2014**, *5*, 4477.
(12) McCrory, C. C. L.; Jung, S.; Peters, J. C.; Jaramillo, T. F. *J. Am. Chem. Soc.* **2013**, *135*, 16977.
(13) Hall, D. E. *J. Electrochem. Soc.* **1983**, *130*, 317.
(14) Trasatti, S. *Electrochim. Acta* **1984**, *29*, 1503.
(15) Li, X.; Walsh, F. C.; Pletcher, D. *Phys. Chem. Chem. Phys.* **2011**, *13*, 1162.
(16) Lyons, M. E. G.; Brandon, M. P. *Int. J. Electrochem. Sci.* **2008**, *3*, 1386.
(17) Lin, F.; Boettcher, S. W. *Nat. Mater.* **2014**, *13*, 81.
(18) Mills, T. J.; Lin, F.; Boettcher, S. W. *Phys. Rev. Lett.* **2014**, *112*, 148304.
(19) Dincă, M.; Surendranath, Y.; Nocera, D. G. *Proc. Natl. Acad. Sci. U. S. A.* **2010**, *107*, 10337.
(20) Bediako, D. K.; Surendranath, Y.; Nocera, D. G. *J. Am. Chem. Soc.* **2013**, *135*, 3662.
(21) Bediako, D. K.; Lassalle-Kaiser, B.; Surendranath, Y.; Yano, J.; Yachandra, V. K.; Nocera, D. G. *J. Am. Chem. Soc.* **2012**, *134*, 6801.
(22) Smith, A. M.; Trotochaud, L.; Burke, M. S.; Boettcher, S. *Chem. Commun.* **2015**, *51*, 5261.
(23) Trotochaud, L.; Young, S. L.; Ranney, J. K.; Boettcher, S. W. *J. Am. Chem. Soc.* **2014**, *136*, 6744.
(24) Trotochaud, L.; Ranney, J. K.; Williams, K. N.; Boettcher, S. W. *J. Am. Chem. Soc.* **2012**, *134*, 17253.
(25) Friebel, D.; Louie, M. W.; Bajdich, M.; Sanwald, K. E.; Cai, Y.; Wise, A. M.; Cheng, M.-J.; Sokaras, D.; Weng, T.-C.; Alonso-Mori, R.; Davis, R. C.; Bargar, J. R.; Norskov, J. K.; Nilsson, A.; Bell, A. T. *J. Am. Chem. Soc.* **2015**, *137*, 1305.
(26) Klaus, S.; Cai, Y.; Louie, M. W.; Trotochaud, L.; Bell, A. T. *J. Phys. Chem. C* **2015**, *119*, 7243.
(27) West, R. C. *Handbook of Chemistry and Physics*, 53rd ed.; CRC Press: Boca Raton, FL, 1972.
(28) House, J. *Inorganic Chemistry*, 2nd ed.; Academic Press: Waltham, 2013; p 358.
(29) Lai, S. C. S.; Kleyn, S. E. F.; Rosca, V.; Koper, M. T. M. *J. Phys. Chem. C* **2008**, *112*, 19080.
(30) Diaz-Morales, O.; Calle-Vallejo, F.; De Munck, C.; Koper, M. T. M. *Chemical Science* **2013**, *4*, 2334.
(31) Gao, P.; Gosztola, D.; Leung, L.-W. H.; Weaver, M. J. *J. Electroanal. Chem. Interfacial Electrochem.* **1987**, *233*, 211.
(32) Trasatti, S.; Petrii, O. A. *J. Electroanal. Chem.* **1992**, *327*, 353.
(33) Nikitenko, S.; Beale, A. M.; Van der Eerden, A. M. J.; Jacques, S. D. M.; Leynaud, O.; O'Brien, M. G.; Detollenaere, D.; Kaptein, R.; Weckhuysen, B. M.; Bras, W. *J. Synchrotron Radiat.* **2008**, *15*, 632.
(34) Filipponi, A.; Di Cicco, A.; Natoli, C. R. *Phys. Rev. B: Condens. Matter Mater. Phys.* **1995**, *52*, 15122.
(35) Filipponi, A.; Di Cicco, A. *Phys. Rev. B: Condens. Matter Mater. Phys.* **1995**, *52*, 15135.
(36) Yeo, B. S.; Bell, A. T. *J. Phys. Chem. C* **2012**, *116*, 8394.
(37) Cornilsen, B. C.; Shan, X.; Loyselle, P. L. *J. Power Sources* **1990**, *29*, 453.
(38) Corrigan, D. A. *J. Electrochem. Soc.* **1989**, *136*, 613.
(39) Nazri, G.; Corrigan, D. A.; Maheswari, S. P. *Langmuir* **1989**, *5*, 17.
(40) Bendert, R. M. *J. Electrochem. Soc.* **1989**, *136*, 1369.
(41) Conell, R. S.; Corrigan, D. A.; Powell, B. R. *Sol. Energy Mater. Sol. Cells* **1992**, *25*, 301.
(42) Yu, P. C.; Lampert, C. M. *Sol. Energy Mater.* **1989**, *19*, 1.
(43) Trotochaud, L.; Mills, T. J.; Boettcher, S. W. *J. Phys. Chem. Lett.* **2013**, *4*, 931.
(44) Lo, Y. L.; Hwang, B. J. *Langmuir* **1998**, *14*, 944.
(45) Hermet, P.; Gourrier, L.; Bantignies, J.-L.; Ravot, D.; Michel, T.; Deabate, S.; Boulet, P.; Henn, F. *Phys. Rev. B: Condens. Matter Mater. Phys.* **2011**, *84*, 235211.
(46) Li, H. B.; Yu, M. H.; Wang, F. X.; Liu, P.; Liang, Y.; Xiao, J.; Wang, C. X.; Tong, Y. X.; Yang, G. W. *Nat. Commun.* **2013**, *4*, 1894.
(47) Desilvestro, J.; Corrigan, D. A.; Weaver, M. J. *J. Phys. Chem.* **1986**, *90*, 6408.
(48) Merrill, M.; Worsley, M.; Wittstock, A.; Biener, J.; Stadermann, M. *J. Electroanal. Chem.* **2014**, *717*−*718*, 177.
(49) Devarajan, V.; Gräfe, E.; Funck, E. *Spectrochimica Acta Part A: Molecular Spectroscopy* **1974**, *30*, 1235.
(50) Devi, S. A.; Philip, D.; Aruldhas, G. *J. Solid State Chem.* **1994**, *113*, 157.
(51) Lewis, J. A. *J. Am. Ceram. Soc.* **2000**, *83*, 2341.
(52) Citra, A.; Chertihin, G. V.; Andrews, L.; Neurock, M. *J. Phys. Chem. A* **1997**, *101*, 3109.
(53) Uzunova, E. L.; Mikosch, H.; Nikolov, G. S. *J. Chem. Phys.* **2008**, *128*, 094307.
(54) Holland, P. L. *Dalton transactions* **2010**, *39*, 5415.
(55) Takashima, T.; Hashimoto, K.; Nakamura, R. *J. Am. Chem. Soc.* **2012**, *134*, 1519.
(56) Diaz-Morales, O.; Ferrus-Suspedra, D.; Koper, M. T. M. Manuscript submitted for publication, **2015**.
(57) Van der Ven, a.; Morgan, D.; Meng, Y. S.; Ceder, G. *J. Electrochem. Soc.* **2006**, *153*, A210.
(58) Risch, M.; Klingan, K.; Heidkamp, J.; Ehrenberg, D.; Chernev, P.; Zaharieva, I.; Dau, H. *Chem. Commun.* **2011**, *47*, 11912.

DOI: 10.1021/jacs.5b06814
J. Am. Chem. Soc. 2015, 137, 15112−15121